ISSN 0021-8944, Journal of Applied Mechanics and Technical Physics, 2021, Vol. 62, No. 7, pp. 1267–1276. © Pleiades Publishing, Ltd., 2021.
Russian Text © The Author(s), 2020, published in Vychislitel'naya Mekhanika Sploshnykh Sred, 2020, Vol. 13, No. 4, pp. 449–458.

Verification of Wide-Range Constitutive Relations for Elastic-Viscoplastic Materials Using the Taylor–Hopkinson Test

Yu. V. Bayandin[a,*], D. R. Ledon[a,], and S. V. Uvarov[a,***]**

[a] *Institute of Continuous Media Mechanics, Ural Branch, Russian Academy of Sciences, Perm, Russia*

**e-mail: buv@icmm.ru*

***e-mail: ledon@icmm.ru*

****e-mail: usv@icmm.ru*

Received September 24, 2020; revised November 26, 2020; accepted December 3, 2020

Abstract—A mathematical model of a solid body with mesoscopic defects is presented and validated. The constitutive relations proposed earlier allow describing the deformation behavior of typical elastic-viscoplastic materials (metals and alloys) in a wide range of strain rates, temperatures, and stresses. Methods for identifying unknown parameters of the model by solving a number of independent optimization problems using data from independent experiments are developed and implemented. For identification we use both the results of a literature review and experimental data. The experimental study on high-speed collision of a cylindrical specimen with an obstacle in the form of a bar (Taylor–Hopkinson test) is carried out by recording the temperature field in the course of deformation. The data are used to verify the model. For comparison the calculations are performed in the three-dimensional statement and in the axisymmetric statement. The formulated boundary value problems are solved numerically by the finite element method. The results of numerical calculations are in good agreement with the experimental data: the shape of the specimen after collision and the measured temperature (mechanical energy dissipation during inelastic deformation) coincide. This confirms the adequacy of the developed mathematical model and indicates that it can be used to solve both fundamental and applied problems of solid mechanics. The analysis of parallelism efficiency shows that the use of eight cores yields a five-fold acceleration and, as the number of cores increases further, this trend presumably continues.

Keywords: metals, alloys, dynamic loading, Hopkinson–Kolsky bar, Taylor test, elastic-viscoplastic constitutive relations

DOI: 10.1134/S0021894421070026

1. INTRODUCTION

It is a topical task of modern machinery and aviation manufacture to predict the strength characteristics of the corresponding structures in their design stage by means of numerical modeling. For this purpose we need development of such constitutive relations (CRs) that allow computing the response of the material to applied loads in a wide range of stresses, strains, and temperatures, including the complex stress–strain state. Building a CR is related with introduction of internal variables and a large number of parameters to be determined. As a rule, the parameters are found from relatively simple experiments on uniaxial tension/compression. However, for adequate description of behavior of real structures, the equations with these parameters must enable computing the three-dimensional stress–strain state. Therefore, the constructed mathematical models are necessarily verified after parameter identification.

One of the ways for verification is the Taylor test [1], which is an experiment consisting in high-speed collision between a bar and a rigid obstacle. In the course of experiment, the inhomogeneous stress–strain state is realized in the bar made of the studied material, and the strain rates achieve 10^5 s^{-1}. This experiment allows determining the mechanical characteristics of material, in particular, the dynamical yield limit [2–4]. By means of this technique the following materials are investigated: titanium alloys [5, 6], steels [7], copper [8, 9], and aluminum alloys [9–11], including porous ones [12]. The model verification includes the calculation corresponding to the experiment and the comparison of the bar shape computed with account for deformation with the shape acquired in the experiment. A similar method of verification

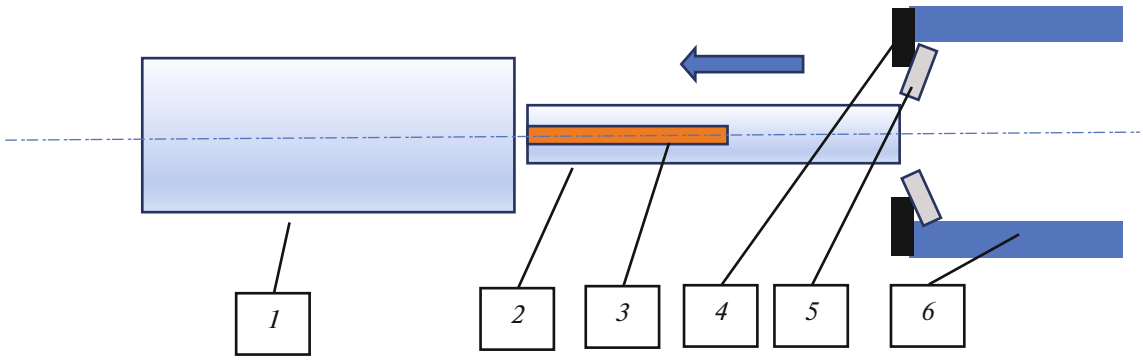

Fig. 1. Scheme of experiment: *1* the steel bar with a diameter of 25 mm, *2* the specimen (impactor), *3* the field of sight of the infrared camera at the specimen surface, *4* shutoff, *5* guideway, and *6* the barrel of the gun; the arrow shows the impact direction.

is widely used for different models: the Johnson–Cook model [13], the Zerilli–Armstrong model [14], the models with linear hardening [2], and other models [8, 15].

The current paper is aimed at checking the adequacy of the proposed solid body model using the Taylor test. The verification is performed on an example of AMg6 alloy, a material widely used in aircraft engine manufacturing.

2. EXPERIMENTAL FORMULATION

The experimental scheme is given in Fig. 1. The specimens had the shape of cylinder with a diameter of 12 mm and a length of 80 mm. To increase the coefficient of the surface radiation of the specimen at its heating (which is required for infrared measurements of the surface temperature), the specimens were covered by a thin layer of soot. To center the specimens in the barrel of the pneumatic gun, we plotted the bottom plates and the guideways on a 3D printer (Fig. 2). The guideway was made so that it easily breaks at the interaction with the shutoff ring mounted at the barrel output and does not intercept the field of view of the infrared camera. The specimen was accelerated in the barrel until the prescribed speed. At collision with the shutoff and destruction, the guideway lost its speed. This allowed recording the surface temperature of the specimen in the field of view of camera *3* (Fig. 1) during 250 μs after the collision between the specimen and the steel bar. We applied the FLIR SC5010 high-speed infrared camera. The range between the frames was 50 μs. The camera was preliminarily calibrated in the temperature range 20–150°C using the test sample as the measurement object. This is caused by the fact that at the chosen framing rate (20 000 frames/s) the range of rising temperatures was a priori outside the range of default camera options. In addition, to avoid large spreading of characteristics of different pixels of the digital camera matrix, we required individual calibration for each pixel. Imaging of specimen *2* was carried out before and during the collision with obstacle *1* (Fig. 1). From the measurement data the surface temperature of the undeformed specimen was 29°C. The alignment of the impact was provided by the bottom plate and guideway *5* made of plastic (Fig. 2); shutoff *4* was applied to ensure visibility in the region where the surface temperature was determined.

The experimental results are presented below together with the calculation results.

Samples made of AMg6 alloy were annealed at a temperature of 500°C over 4 hours. This regime was selected by the results of study [16], where it was established that, with differential scanning calorimetry of deformed specimens made of this alloy, the release of the energy accumulated during plastic deformation is terminated at temperatures of 350–400°C.

3. SYSTEM OF FIELD EQUATIONS

The complete system of field equations for describing the deformation behavior of material has the form

$$\rho\dot{\mathbf{v}} = \nabla\cdot\boldsymbol{\sigma}, \tag{1}$$

$$\dot{\rho} + \rho\nabla\cdot\mathbf{v} = 0, \tag{2}$$

$$\mathbf{D} = \frac{1}{2}(\nabla\mathbf{v} + \nabla\mathbf{v}^{\mathrm{T}}), \tag{3}$$

$$\boldsymbol{\sigma} = \boldsymbol{\sigma}_s + \boldsymbol{\sigma}_d, \qquad \boldsymbol{\sigma}_s = \frac{1}{3}(\boldsymbol{\sigma} : \mathbf{E})\mathbf{E}, \tag{4}$$

$$\boldsymbol{\sigma}^R = \lambda(\mathbf{D} : \mathbf{E})\mathbf{E} + 2G(\mathbf{D} - \dot{\boldsymbol{\varepsilon}}^p - \dot{\mathbf{p}}), \tag{5}$$

$$\boldsymbol{\sigma}^R = \dot{\boldsymbol{\sigma}} - \dot{\mathbf{R}} \cdot \mathbf{R}^{\mathrm{T}} \cdot \boldsymbol{\sigma} + \boldsymbol{\sigma} \cdot \dot{\mathbf{R}} \cdot \mathbf{R}^{\mathrm{T}}, \tag{6}$$

$$\dot{\boldsymbol{\varepsilon}}^p = \dot{\varepsilon}_0^{n_\varepsilon} \exp\left(\frac{U(T)}{kT}\right)\left(\Gamma_\sigma\boldsymbol{\sigma} - \Gamma_{p\sigma}\frac{\partial F}{\partial \mathbf{p}}\right), \tag{7}$$

$$\dot{\mathbf{p}} = \dot{\varepsilon}_0^{n_p} \exp\left(\frac{U(T)}{kT}\right)\left(\Gamma_{p\sigma}\boldsymbol{\sigma} - \Gamma_p\frac{\partial F}{\partial \mathbf{p}}\right), \tag{8}$$

$$U(T) = \frac{k}{T_c^m}T^{m+1}, \tag{9}$$

$$\frac{F}{F_m} = \frac{p^2}{2} - \frac{p^2}{2\delta} + c_1 p + c_2 \ln(c_3 + c_4 p + p^2) - \frac{\boldsymbol{\sigma}_d : \mathbf{p}}{2G}, \tag{10}$$

$$\rho c\dot{T} = \boldsymbol{\sigma} : \dot{\boldsymbol{\varepsilon}}^p - \frac{\partial F}{\partial \mathbf{p}} : \dot{\mathbf{p}} + \alpha\Delta T. \tag{11}$$

In expressions (1)–(11) we use the following denotations: ρ is the mass density, $\mathbf{v}$ is the velocity vector (a dot above the symbol means the material derivative of this variable), $\boldsymbol{\sigma}$, $\boldsymbol{\sigma}_s$, and $\boldsymbol{\sigma}_d$ is the stress tensor and its spherical and deviatoric parts, $\nabla(\cdot)$ is the gradient operator in the current configuration, $\mathbf{D}$ is the strain rate tensor, $\boldsymbol{\varepsilon}^p$ is the plastic strain tensor, λ and G are elastic moduli of material, $\mathbf{E}$ is the identity tensor, $\dot{\varepsilon}_0 = \sqrt{(2/3)\mathbf{D} : \mathbf{D}}/\dot{\varepsilon}_c$ is the strain rate intensity, $\dot{\varepsilon}_c = 1\ \mathrm{s}^{-1}$, is the nondimensionalization factor, k is the Boltzmann constant, Γ_σ, $\Gamma_{p\sigma}$, and Γ_p are positive kinetic coefficients, n_ε and n_p are constants responsible for strain rate sensitivity of the material, F is the potential of the nonequilibrium Helmholtz free energy, $\mathbf{p}$ is the tensor of microshear density, $p = \sqrt{\mathbf{p} : \mathbf{p}}$ is the microshear intensity, c is the specific heat capacity, α is the heat transfer coefficient, T is the temperature, $\Delta(\cdot)$ is the Laplace operator, F_m, δ, and $c_1 - c_4$ are approximation constants of the Helmholtz free energy F, T_c and m are approximation constants of the characteristic energy of activation U, and $\mathbf{R}$ is the orthogonal tensor of the polar decomposition of the deformation gradient $\mathbf{F} = \mathbf{R} \cdot \mathbf{U}$, where $\mathbf{U}$ is the right symmetric positive definite distortion tensor.

The wide-range constitutive relations (5), (7), and (8) were proposed in the general form in [17]. The structure of the equations and the approximation for the potential of the nonequilibrium free energy (10) were proposed in [18, 19]. In [20, 21] the dependences for the characteristic relaxation times were described. In work [22] the authors specified the form of approximation for the energy of activation (9).

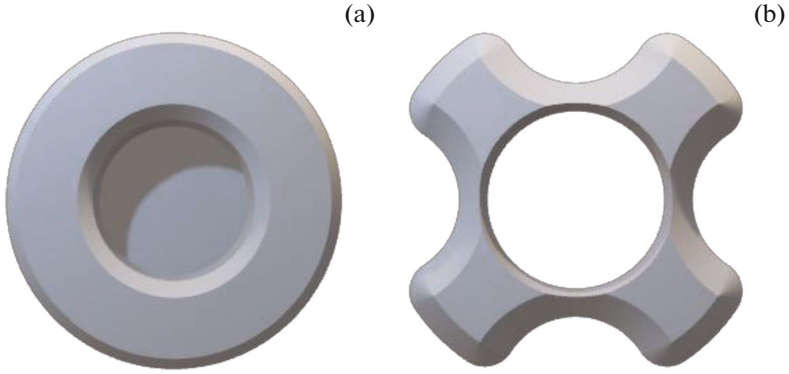

Fig. 2. Shapes of (a) bottom plate and (b) guideway for the specimen.

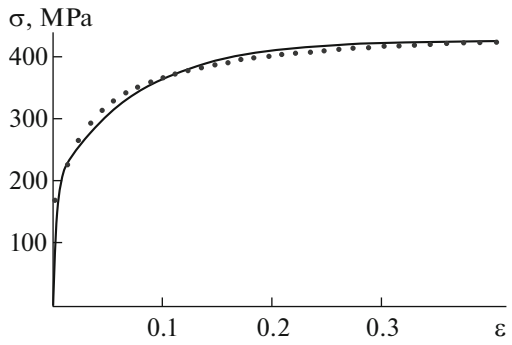

Fig. 3. Calculation (solid line) and experimental (dotted line) strain diagrams.

In [23] the fractions of dissipated and stored energy of inelastic deformation (11) were determined. The relations used for Hooke's law (5) were justified in [24], and the relations for the objective Green–Naghdi derivative (6) in elastic-viscoplastic relations were justified in work [25].

4. IDENTIFICATION OF MODEL PARAMETERS

The kinetic coefficients Γ_σ, $\Gamma_{p\sigma}$, and Γ_p were determined from the solution of the minimization problem of the residue between the experimental and the calculated strain diagrams at a characteristic strain rate of 1 s^{-1} and a temperature of 25°C. The result of the numerical modeling compared with the experimental data is given in Fig. 3. In plotting diagrams we used the logarithmic strain measure and the true stresses.

The parameters responsible for strain rate sensitivity of material (n_ε and n_p) were determined by the experimental values of the yield limit at different strain rates. The initial data are the values of the kinetic coefficients obtained at the previous step. The tests were performed at a temperature of 25°C. As the yield limit, we took the stress for the inelastic strain value of 0.2%. The result is presented in Table 1.

The constants responsible for the thermal softening (T_c and m) were identified by solving the problem of minimization of the difference between the experimental and calculated yield limits at a characteristic strain rate of 1 s^{-1} and different temperatures. The results are contained in Table 2.

The complete set of constants for the AMg6 alloy is listed below:

–The constants known from the literature [27]: $\rho = 2640$ kg/m^3, $\lambda = 41$ GPa, $G = 27$ GPa, $c = 922$ J/(kg K), and $\alpha = 122$ W/(m K).

–The identified constants: $\Gamma_\sigma = 3.36\times10^{-9}$ (Pa s)$^{-1}$, $\Gamma_{p\sigma} = 0.52\times10^{-9}$ (Pa s)$^{-1}$, and $\Gamma_p = 0.27\times10^{-9}$ (Pa s)$^{-1}$; $n_\varepsilon = n_p = 0.985$, $T_c = 287$°C, $m = 2$.

–The approximation constants of the thermodynamic potential F: $c_1 = -0.00535972$, $c_2 = 0.519$, $c_3 = 0.581$, $c_4 = 0.006$, and $\delta = 1.15$; the value of the constant c_1 is computed exactly from the equation $c_1 = -\dfrac{c_2c_4}{c_3}$ following from the condition $\left.\dfrac{\partial F}{\partial p}\right|_{p=0,\sigma=0} = 0$.

The bar which, in contrast to the impactor made of AMg6, is made of high-strength martensite-aging steel 02N18K9M5T-VI ($\sigma_u = 1.91$ GPa), was described by the constitutive relations of the linear theory of

Table 1. Calculated and experimental yield limits at different strain rates

Strain rate, s^{-1}	Yield limit (calculation), MPa	Yield limit (experiment), MPa	Source of experimental data
1	164	165	This work
520	176	175	[26]

Table 2. Calculated and experimental yield limits at different temperatures

Temperature, °C	Yield limit (calculation), MPa	Yield limit (experiment [27]), MPa	Relative error, %
25	164	165	0.6
100	153	160	4.4
200	117	135	13.3
300	72	60	16.7

elasticity. The constants for the bar materials were as follows: $\rho = 7800$ kg/m^3, $E = 210$ GPa is Young's modulus, and $\nu = 0.28$ is the Poisson coefficient.

5. BOUNDARY CONDITIONS

The geometry of the problem in axisymmetric formulation is depicted in Fig. 4. At the initial time instance, the specimen-impactor tightly fit the bar-obstacle. For the entire volume of the specimen V_p, the initial speed of collision $v_x|_{V_p} = v_0 = -156$ m/s measured in the experiment is known; in the radial direction the speed is zero: $v_r|_{V_p} = 0$ m/s, and the initial temperature is equal to room temperature: $T|_{V_p} = T_0 = 29$°C. The bar has zero initial speed.

We prescribe the conditions at the boundaries:

–At S_a we prescribe the symmetry conditions $u_r|_{S_a} = 0$ and $t_x|_{S_a} = 0$. Here, $\mathbf{u} = \{u_x, u_r\}$ is the displacement vector, $\mathbf{v} = \dot{\mathbf{u}}$, $\mathbf{t} = \{t_x, t_r\} = \boldsymbol{\sigma} \cdot \mathbf{n}$ is the force vector, and $\mathbf{n} = \{n_x, n_r\}$ is the normal vector to the surface.

–At S_b we do not allow displacements along the x axis: $u_x|_{S_b} = 0$ and $t_r|_{S_b} = 0$.

–At S_f we prescribe the free surface condition $\boldsymbol{\sigma} \cdot \mathbf{n}|_{S_f} = 0$.

–At S_c we prescribe the condition of contact interaction: $(\boldsymbol{\sigma} \cdot \mathbf{n}) \cdot \boldsymbol{\tau}|_{S_c} = \mu (\boldsymbol{\sigma} \cdot \mathbf{n}) \cdot \mathbf{n}|_{S_c}$, where $\boldsymbol{\tau} = \{\tau_x, \tau_r\}$ is the tangent vector to the surface and μ is the friction coefficient.

–At the entire boundary of the impactor, the adiabatic conditions are fulfilled: $\nabla_n T|_{\partial V_p} = \mathbf{0}$, where the operator $\nabla_n \equiv \mathbf{nn} \cdot \nabla$ defines the projection to the normal $\mathbf{n}$ and the dyad $\mathbf{nn}$ is the projector.

The geometry of the calculation domain of the problem in the three-dimensional formulation is drawn in Fig. 5.

The boundary conditions of the three-dimensional formulation are analogous to the axisymmetric one, except for the conditions at the axis of symmetry:

–The initial conditions are $v_x|_{V_p} = v_0 = -156$ m/s, $v_y|_{V_p} = 0$ m/s, $v_z|_{V_p} = 0$ m/s, $T|_{V_p} = T_0 = 29$°C.

–The boundary conditions are: $u_x|_{S_b} = 0$, $t_r|_{S_b} = 0$, $\boldsymbol{\sigma} \cdot \mathbf{n}|_{S_f} = 0$, $(\boldsymbol{\sigma} \cdot \mathbf{n}) \cdot \boldsymbol{\tau}|_{S_c} = \mu (\boldsymbol{\sigma} \cdot \mathbf{n}) \cdot \mathbf{n}|_{S_c}$, $\nabla_n T|_{\partial V_p} = \mathbf{0}$, $\mathbf{u} = \{u_x, u_y, u_z\}$, $\mathbf{t} = \{t_x, t_y, t_z\} = \boldsymbol{\sigma} \cdot \mathbf{n}$, $\mathbf{n} = \{n_x, n_y, n_z\}$, and $\boldsymbol{\tau} = \{\tau_x, \tau_y, \tau_z\}$.

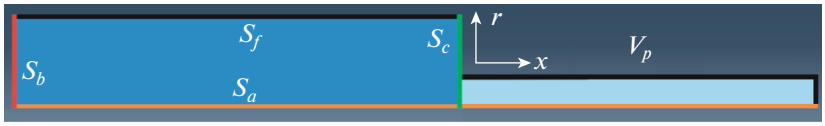

Fig. 4. Geometry of calculation domain for axisymmetric problem.

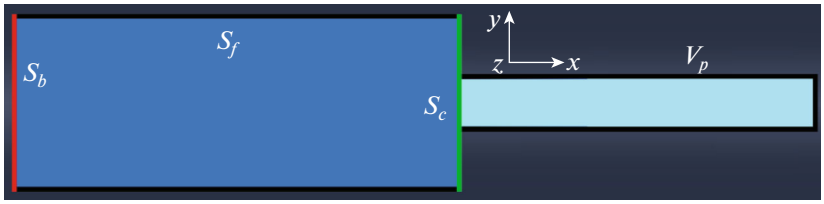

Fig. 5. Geometry of calculation domain for three-dimensional problem.

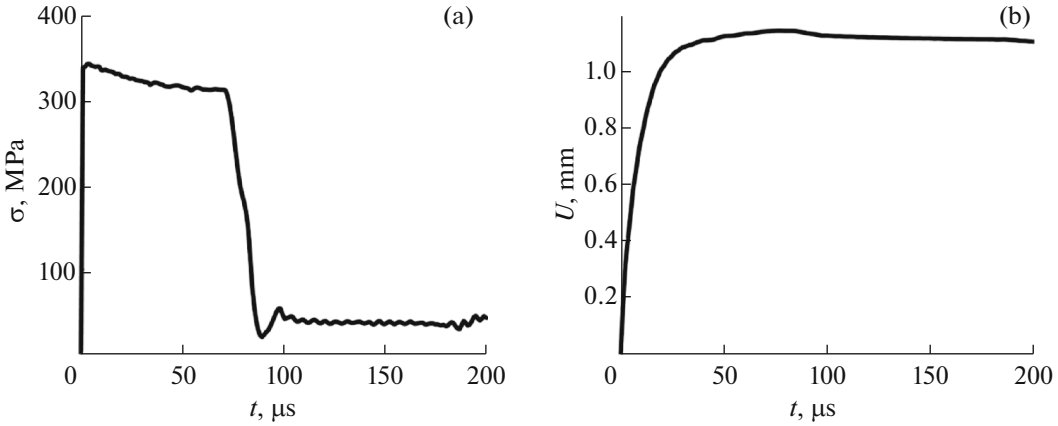

Fig. 6. (a) Von Mises stress and (b) radial displacements at face end of impactor over time.

6. RESULTS OF NUMERICAL MODELING

Problem (1)–(11) in combination with the boundary conditions was solved numerically using the finite element method. The constitutive relations were implemented in the VUMAT procedure in the incremental form by means of the explicit integration scheme with automatic selection of the time step included in the Abaqus\Explicit solver and showed its efficiency in dynamic problems. The area of numerical integration was covered by the uniform mesh with a characteristic spatial approximation size of 0.25 mm (for the impactor) and 5 mm (for the bar) in the three-dimensional formulation and 0.1 mm (for the impactor) and 10 mm (for the bar) in the axisymmetric formulation. In the three-dimensional case we used the hexagonal elements, and in the axisymmetric case we used the quadrilateral finite elements. The time integration step has an order of 10^{-8} s.

The time period for computations was 200 μs. We established that this interval is sufficient to bring the specimen and the bar to the state of relative equilibrium. We see in Fig. 6 that the radial displacements at the face end of the impactor reach the stationary values at the mentioned time instance, and the stresses become small, not capable of further significant deformations. After that, in comparison with the experimental data, the calculation results are presented at the end of tests at a time instance of 200 μs.

The radial displacements obtained in the calculations and in the experiment are presented in Fig. 7. Their comparison shows good qualitative and quantitative agreement. The maximum relative error was 7%.

Figure 8 contains the temperature distribution over the bar surface measured in the experiment and obtained in the calculations. Disagreement of the values at the face end may be associated with several reasons. Firstly, the spatial resolution of the infrared camera is far less than the spatial discretization in the numerical model. Therefore, it is not excluded that temperature peak was not caught. Secondly, the camera could not record the temperature at the face end because of technical difficulties in contact interaction between cylinders of unequal diameter (the impactor and the bar): due to imaging at a distance at a certain angle, the face end of the bar may be intercepted by the impactor face end. Hence, the values at the face end are not taken into account in computing the error. The error could also be caused by disallowing the thermoelastic effect in Eq. (11); however, it makes a negligible contribution. The largest error is observed at a distance of 8–20 mm from the face end (Fig. 8). At the same distance the calculation provides the underestimated displacement value (Fig. 7); consequently, the strains are also underestimated which leads

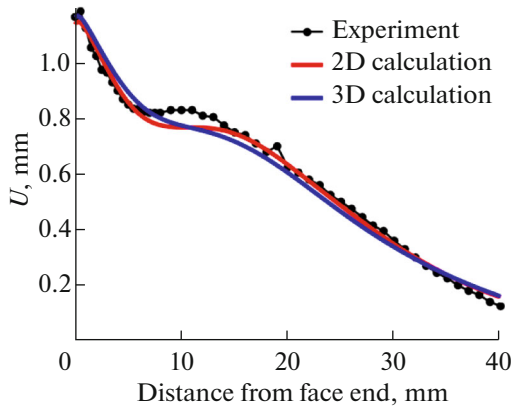

Fig. 7. Radial displacements after collision along impactor.

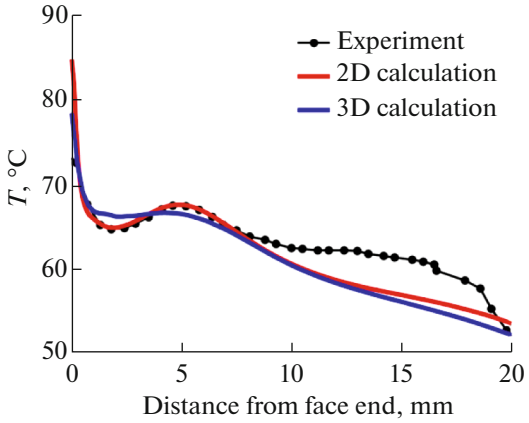

Fig. 8. Temperature at impactor surface after collision over its length.

to an underestimated temperature value obtained from Eq. (11). The relative error in computing the temperature was 11%.

In the course of collision, different strain rates are realized in different regions of the impactor. For instance, at the beginning of the impact, near the face end they reach values from 2×10^4 to 10^5 s^{-1} (Fig. 9), which is substantially higher than the strain rates at which the model parameters were identified (520 s^{-1}). Nevertheless, the final shape of the impactor is described with high accuracy. This indicates that the proposed model has not only descriptive, but also the predictive capabilities. In addition, we observe the characteristic conical configuration (the results in Fig. 9 are presented for the axisymmetric problem), which is typical at loading cylindrical specimens both in quasi-static and in dynamic experiments. The difference from the standard compression tests of cylinders, in which the distribution has the form of a double cone with an intersection at the center of the specimen, consists in the fact that in the Taylor test the inelastic deformation begins to develop from the side of impact (from the left face end of the specimen, see Fig. 9); therefore, the apex of the cone is situated also at the specimen face end.

In Fig. 10, we present the calculation results without accounting for the strain rate sensitivity (at $n_\varepsilon = n_p = n = 1$). We see that in this case the calculation quantitatively does not agree with the experiment (the relative error is 15%). The results agree only on the segment from 30 to 40 mm, where the strain rates are low (close to 1 s^{-1}). This confirms the necessity of accounting for the hardening by increasing the strain rate and illustrates the capability of the proposed model to describe the hardening in a wide range of strain rates.

We additionally analyzed the efficiency of parallelization of computations in solving the formulated problem. In Fig. 11, we depict the graph of computation acceleration dependent on the number of pro-

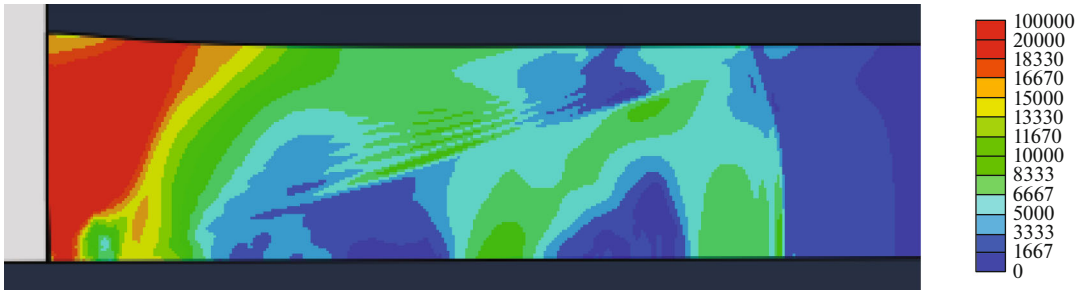

Fig. 9. Distribution of strain rate (s^{-1}) at time instance $t = 4$ μs.

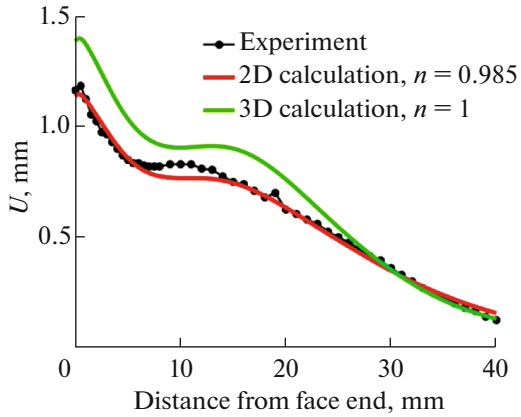

Fig. 10. Radial displacements along impactor after collision with/without accounting for the strain rate sensitivity of the material.

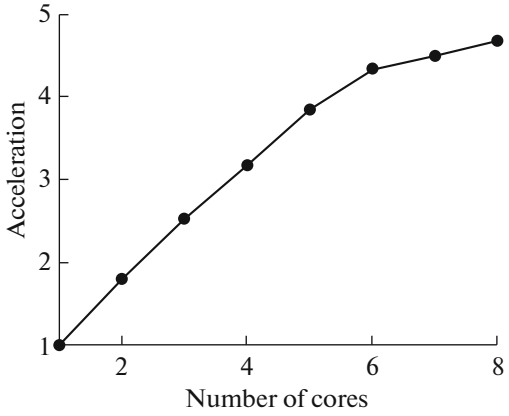

Fig. 11. Calculation acceleration over number of used cores.

cessing cores. The capability of parallelization of computations is very important, especially when we deal with the design and strength estimation of real structures. Such problems contain large integration regions and their complex configuration sometimes requires detailed partitioning into finite elements, which leads to immense time costs for the solution. With a low number of computation cores, we observe a linear growth in the computation acceleration value, and then a reduction in the efficiency of parallelization.

7. CONCLUSIONS

In this work, we implemented dynamic experiments in the statement of the Taylor–Hopkinson test with simultaneous recording of the surface temperature of the specimen, which we subsequently used for

verifying the mathematical model of elastic-viscoplastic materials (metals and alloys) developed at the Physical Foundations of Strength Laboratory, Institute of Continuous Media Mechanics, Ural Branch, Russian Academy of Sciences. The constructed wide-range constitutive relations for a solid body with defects take into account the accumulation of defects (microshears) and dissipation of energy by means of inelastic deformation. The procedure for identifying the model parameters responsible for inelastic deformation of the material was executed in several stages using the data of uniaxial quasi-static loading (shortening of a cylindrical specimen) and of dynamic tests (of the Hopkinson–Kolsky bar).

The boundary value problem about the collision between a cylindrical specimen made of AMg6 and a steel bar (in the formulation of the Taylor–Hopkinson test) was solved numerically by the finite element method in the axisymmetric and three-dimensional statements. We obtained good agreement between the results of numerical modeling and the experimental data; the error in the radial displacements was 7%, and the error in the temperature, 11%. Thus, we may conclude that the mathematical model of the behavior of a deformable solid body under quasi-static and dynamic loads is adequate and the developed constitutive relations allow describing the deformation of materials in a wide range of strain rates including accounting for damage accumulation (microshear) and energy dissipation.

FUNDING

The work is supported by the State Task of the Ministry of Science and Higher Education of the Russian Federation (project no. AAAA-A19-119013090021-5).

REFERENCES

1. Taylor, G.I., The use of flat-ended projectiles for determining dynamic yield stress, *Proc. R. Soc. London, Ser. A,* 1948, vol. 3, pp. 289–301. https://doi.org/10.1098/rspa.1948.0081
2. Bragov, A.M., Konstantinov, A.Yu., and Lomunov, A.K., *Eksperimental'no-teoreticheskoe issledovanie protsessov vysokoskorostnogo deformirovaniya i razrusheniya materialov razlichnoy fizicheskoi prirody s ispol'zovaniem metoda Kol'skogo i ego modifikatsii* (Experimental and Theoretical Study of the Processes of High-Speed Deformation and Fracture of Materials of Various Physical Nature Using the Kolsky Method and Its Modifications), Nizh. Novgorod: NNGU im. N.I. Lobachevskogo, 2018.
3. Sen, S., Banerjee, B., and Shaw, A., Taylor impact test revisited: Determination of plasticity parameters for metals at high strain rate, *Int. J. Solid Struct.,* 2020, vol. 193–194, pp. 357–374. https://doi.org/10.1016/j.ijsolstr.2020.02.020
4. Bogomolov, A.I., Gorel'skii, V.A., Zelepugin, S.A., and Khorev, I.E., Behavior of bodies of revolution in dynamic contact with a rigid wall, *J. Appl. Mech. Tech. Phys.,* 1986, vol. 27, pp. 149–152. https://doi.org/10.1007/BF00911139
5. Chandola, N., Revil-Baudard, B., and Cazacu, O., Plastic deformation of high-purity α-titanium: Model development and validation using the Taylor cylinder impact test, *J. Phys.: Conf. Ser.,* 2016, vol. 734, p. 032048. https://doi.org/10.1088/1742-6596/734/3/032048
6. Holt, W.H., Mock, W., Zerilli, F.J., and Clark, J.B., Experimental and computational study of the impact deformation of titanium Taylor cylinder specimens, *Mech. Mater.,* 1994, vol. 17, pp. 195–201. https://doi.org/10.1016/0167-6636(94)90059-0
7. Rakvag, K.G., Borvik, T., and Hopperstad, O.S., A numerical study on the deformation and fracture modes of steel projectiles during Taylor bar impact tests, *Int. J. Solid Struct.,* 2014, vol. 51, pp. 808–821. https://doi.org/10.1016/j.ijsolstr.2013.11.008
8. Borodin, E.N. and Mayer, A.E., Structural model of mechanical twinning and its application for modeling of the severe plastic deformation of copper rods in Taylor impact tests, *Int. J. Plast.,* 2015, vol. 74, pp. 141–157. https://doi.org/10.1016/j.ijplas.2015.06.006
9. Bartkowski, P., Keele, M., and Bruchey, W., in *Proceedings of the 19th International Symposium of Ballistics, Interlaken, Switzerland, May 7–11, 2001,* vol. 3, pp. 1577–1584.
10. Mocko, W., Janiszewski, J., Radziejewska, J., and Grazka, M., Analysis of deformation history and damage initiation for 6082-T6 aluminium alloy loaded at classic and symmetric Taylor impact test conditions, *Int. J. Impact Eng.,* 2015, vol. 75, pp. 203–213. https://doi.org/10.1016/j.ijimpeng.2014.08.015
11. Wei, G., Zhang, W., Huang, W., Ye, N., Gao, Y., and Ni, Y., Effect of strength and ductility on deformation and fracture of three kinds of aluminum alloys during Taylor tests, *Int. J. Impact Eng.,* 2014, vol. 73, pp. 75–90. https://doi.org/10.1016/j.ijimpeng.2014.06.011

12. Belov, G.V., Gusarov, A.P., Markov, V.A., Pusev, V.A., Ovchinnikov, A.F., Selivanov, V.V., and Sotskiy, M.Yu., Application of the Taylor test to research dynamic mechanical properties of highly porous aluminum alloy, *Nauka Obrazov.,* 2012, no. 9, pp. 13–28.
https://doi.org/10.7463/0912.0442058

13. Kleiser, G., Revil-Baudard, B., and Pasiliao, C., High strain-rate plastic deformation of molybdenum: Experimental investigation, constitutive modeling and validation using impact tests, *Int. J. Impact Eng.,* 2016, vol. 96, pp. 116–128.
https://doi.org/10.1016/j.ijimpeng.2016.05.019

14. Zerilli, F.J. and Armstrong, R.W., Dislocation-mechanics based constitutive relations for material dynamics calculations, *J. Appl. Phys.,* 1987, vol. 61, pp. 1816–1825.
https://doi.org/10.1063/1.338024

15. Maudlin, P.J., Bingert, J.F., House, J.W., and Chen, S.R., On the modeling of the Taylor cylinder impact test for orthotropic textured materials: Experiments and simulations, *Int. J. Plast.,* 1999, vol. 15, pp. 139–166.
https://doi.org/10.1016/S0749-6419(98)00058-8

16. Efremov, D.V., Uvarov, S.V., Spivak, L.V., and Naimark, O.B., Statistical patterns of deformation localization during plastic flow in the AMg_6 alloy, *Pis'ma Mater.,* 2020, vol. 10, no. 1 (37), pp. 38–42.
https://doi.org/10.22226/2410-3535-2020-1-38-42

17. Naimark, O.B., Collective properties of defects ensembles and some nonlinear problems of plasticity and fracture, *Phys. Mesomech.,* 2003, vol. 6, no. 4, pp. 39–63.

18. Bayandin, Yu., Leont'ev, V., Naimark, O., and Permjakov, S., Experimental and theoretical study of universality of plastic wave fronts and structural scaling in shock loaded copper, *J. Phys. IV* (France), 2006, vol. 134, pp. 1015–1021.
https://doi.org/10.1051/jp4:2006134155

19. Bayandin, Yu.V., Saveleva, N.V., Savinykh, A.S., and Naimark, O.B., Numerical simulation of multiscale damage-failure transition and shock wave propagation in metals and ceramics, *J. Phys.: Conf. Ser.,* 2014, vol. 500, p. 152001.
https://doi.org/10.1088/1742-6596/500/15/152001

20. Saveleva, N., Bayandin, Yu., and Naimark, O., Wide-range simulation of elastoplastic wave fronts and failure of solids under high-speed loading, *AIP Conf. Proc.,* 2015, vol. 1683, p. 020201.
https://doi.org/10.1063/1.4932891

21. Saveleva, N.V., Bayandin, Y.V., Savinykh, A.S., Garkushin, G.V., Lyapunova, E.A., Razorenov, S.V., and Naimark, O.B., Peculiarities of the elastic-plastic transition and failure in polycrystalline vanadium under shock-wave loading conditions, *Tech. Phys. Lett.,* 2015, vol. 41, pp. 579–582.
https://doi.org/10.1134/S1063785015060292

22. Bilalov, D.A., Bayandin, Yu.V., and Naimark, O.B., Mathematical modeling of failure process of AlMg2.5 alloy in high and very high cycle fatigue, *J. Appl. Mech. Tech. Phys.,* 2019, vol. 60, pp. 1209–1219.
https://doi.org/10.1134/S0021894419070022

23. Kostina, A.A., Bayandin, Yu.V., and Plekhov, O.A., Model of energy accumulation and dissipation in plastically deformed metals, *Fiz. Mezomekh.,* 2014, vol. 17, no. 1, pp. 43–49.

24. Annin, B.D. and Korobeynikov, S.N., Admissible forms of elastic deformation laws in the determining elastic-plasticity relations, *Sib. Zh. Ind. Mat.,* 1998, vol. 1, no. 1, pp. 21–34.

25. Novokshanov, R.S. and Rogovoy, A.A., On the construction of evolutionary constitutive equations, *Vestn. PNIPU, Mat. Model. Sist. Protsess.,* 2001, no. 9, pp. 103–109.

26. Glushak, B.L., Ignatova, O.N., Pushkov, V.A., Novikov, S.A., Girin, A.S., and Sinitsyn, V.A., Dynamic deformation of aluminum alloy AMg-6 at normal and higher temperatures. *J. Appl. Mech. Tech. Phys.,* 2000, vol. 41, pp. 1083–1086.
https://doi.org/10.1023/A:1026662824249

27. *Mashinostroenie, Entsiklopediya, Tom II-3: Tsvetnye metally i splavy. Kompozitsionnye metallicheskie materialy* (Mechanical Engineering, Encyclopedia, Vol. II-3: Non-Ferrous Metals and Alloys. Composite Metallic Materials), Fridlyander, I.N., Ed., Moscow, Mashinostroenie, 2001.

Translated by E. Oborin